High Entropy Materials and Energies
https://www.sciltp.com/journals/heme

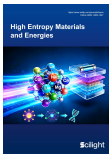

Article

Check for updates

Phase Chemistry and Spatial Organization Govern Chloride Corrosion Behavior of CrFeNi-Based Multi-Principal Element Alloys

Qingwei Gao *, Changzi Chen, Jianfei Wang, Huiqiang Huang and Xiaoming Yang

College of Intelligent Manufacturing, Jingchu University of Technology, Jingmen 448000, China
* Correspondence: gaoqingweisdu@163.com or gaoqingwei@jcut.edu.cn

How To Cite: Gao, Q.; Chen, C.; Wang, J.; et al. Phase Chemistry and Spatial Organization Govern Chloride Corrosion Behavior of CrFeNi-Based Multi-Principal Element Alloys. *High Entropy Materials and Energies* **2026**, *1*(1), 8. https://doi.org/10.53941/heme.2026.100008

Received: 1 October 2026
Revised: 23 October 2026
Accepted: 4 November 2026
Published: 16 November 2026

Abstract: Phase heterogeneity provides an effective strategy for designing multi-principal element alloys (MPEAs), yet how phase constitution and spatial organization regulate chloride corrosion remains insufficiently understood. Here, the electrochemical corrosion behavior of as-cast equiatomic CrFeNi (AC-CrFeNi), as-cast $Cr_{30}Fe_{30}Ni_{30}Al_5Ti_5$ (AC-CrFeNiAlTi), and hot-rolled $Cr_{30}Fe_{30}Ni_{30}Al_5Ti_5$ (HR-CrFeNiAlTi) was comparatively investigated in 3.5 wt.% NaCl solution. The Al/Ti-induced transition from a single-phase FCC structure to a face-centered cubic (FCC) and body-centered cubic (BCC) heterogeneous architecture containing hierarchical ordered precipitates reduced the corrosion current density from 15.15 to 9.302 μA cm^{-2} and increased the low-frequency impedance modulus from 9.457 to 16.702 kΩ cm^2. Further reorganization of the FCC/BCC regions into a directional lamellar morphology at unchanged nominal composition enhanced the corrosion resistance, yielding an icorr of 6.47 μA cm^{-2} and |Z|0.01 Hz of 47.176 kΩ cm^2. Electrochemical impedance analysis revealed that the improved corrosion response of the hot-rolled alloy was accompanied by a more capacitive interfacial response and prolonged relaxation behavior. Post-electrochemical characterization revealed localized oxygen-enriched corrosion products, while XRD confirmed the retention of the primary FCC structure in AC-CrFeNi and the FCC/BCC structures in both CrFeNiAlTi conditions, indicating that corrosion remained controlled by microstructurally dependent local attack rather than extensive phase degradation. The results reveal that chloride corrosion in CrFeNi-based MPEAs is governed by the coupling between phase chemistry, local electrochemical heterogeneity, and phase morphology. This work highlights that reorganizing heterogeneous phase architectures provides a viable pathway for simultaneously tailoring mechanical and corrosion performance in advanced MPEAs.

Keywords: multi-principal element alloy; phase heterogeneity; microstructural morphology; electrochemical corrosion; localized corrosion

1. Introduction

Multi-principal element alloys (MPEAs) provide an unusually broad compositional space for tailoring phase stability, microstructure, and service performance, but this chemical complexity also makes their aqueous corrosion behavior intrinsically structure-sensitive [1–4]. Current reviews agree that nominal composition alone is insufficient to predict corrosion because elemental partitioning, local chemical order, secondary phases, inclusions, interfaces, and passive-film evolution can all alter the electrochemical response [1–4]. At the atomic and surface-film scales, recent studies further show that changes in chemical short-range order or Al-assisted

Copyright: © 2026 by the authors. This is an open access article under the terms and conditions of the Creative Commons Attribution (CC BY) license (https://creativecommons.org/licenses/by/4.0/).
Publisher's Note: Scilight stays neutral with regard to jurisdictional claims in published maps and institutional affiliations.

passivation can modify Cr-centered passive-film chemistry and kinetics even when the overall alloy family remains similar [5,6]. The central issue is therefore not simply whether an MPEA contains corrosion-resistant elements, but how those elements are distributed among phases and represented in the electrochemically active surface film.

Cr-Fe-Ni- and Co-Cr-Ni-based concentrated alloys provide a useful platform for examining this problem because Cr promotes passivation while alloying and phase separation readily redistribute Cr, Ni, Fe, and other additions. In CoCrNi-based alloys, Mo addition and other microstructural changes can substantially modify corrosion current and impedance [7,8], whereas chemically distinct inclusions may become preferential sites for localized attack even in an otherwise face-centered cubic (FCC)-dominated alloy [9]. Passivation studies of CoCrFeNiMo-based alloys likewise demonstrate that the protective response depends on the chemical constitution of the surface film rather than on bulk Cr content alone [10]. A similar structure dependence is evident in $CrFeNi_2$-based and $Al_xCrFeNi_{3-x}$ alloys: changing from a single FCC state to FCC/B2 or eutectic multiphase structures changes both passivation and localized-corrosion behavior [11,12]. These observations show that phase formation and local partitioning must be considered together when evaluating corrosion in Cr/Ni-rich MPEAs.

This requirement becomes particularly important when Al and Ti are introduced for precipitation strengthening. Aging of $(FeCoNi)_{86}Al_7Ti_7$ alloys changes the size, distribution, and chemistry of ordered precipitates and simultaneously alters corrosion resistance [13,14], demonstrating that precipitation strengthening does not have a unique electrochemical consequence. Al/Ti co-alloying in CoCrFeNi-based alloys can provide a favorable strength-corrosion balance under selected microstructural conditions [15], and a precipitation-strengthened $Ni_{34}Co_{28}Cr_{28}Al_{10}$ MPEA was also reported to retain strong corrosion resistance [16]. Conversely, studies of compositionally complex Al-Cr-Fe-Ni-Ti/Mo alloys show that localized corrosion can remain strongly phase-dependent when constituent phases develop different passive-film chemistry [17,18]. Thus, ordered precipitates and multiphase structures should not be treated as intrinsically beneficial or detrimental; their effect depends on phase chemistry, elemental partitioning, and the electrochemical contrast established between neighboring regions.

Beyond phase identity, the spatial arrangement of the phases is increasingly recognized as an independent variable. In Cr-Fe-Ni-Nb eutectic alloys, changes in eutectic constitution and interphase spacing alter localized corrosion and passivation [19,20]. More recently, a systematic AlxFeNiCrCo study showed that corrosion could not be correlated with body-centered cubic (BCC) fraction or grain size alone because FCC/BCC morphology and passive-film defects evolved concurrently [21]. A multi-level heterogeneous lamellar eutectic high-entropy alloy further exhibited a corrosion response distinct from its less organized counterpart, directly linking lamellar heterogeneity with the distribution and development of corrosion damage [22]. Collectively, these studies indicate that continuity, aspect ratio, interphase spacing, and interfacial density can regulate how chemically different regions interact with the electrolyte and with one another. Phase morphology therefore deserves to be examined separately from phase fraction whenever possible.

Thermomechanical processing offers a practical means of changing phase morphology, but it also creates an interpretation challenge because several structural variables often change simultaneously. In a precipitation-strengthened CoCrNi-based alloy, thermomechanical processing modified both the microstructure and chloride corrosion response [23]. Grain-boundary engineering of $Al_{0.3}CoCrFeNi_{1.5}$ likewise improved corrosion resistance through processing-induced changes in boundary character and microstructural state [24]. Such studies establish that processing matters, but they do not fully separate the effects of phase morphology from the other microstructural changes introduced by processing. A more informative comparison therefore uses the same nominal composition with distinctly different phase arrangements, while recognizing that phase fractions and defect structures may also change.

In our previous work, a Co-free $Cr_{30}Fe_{30}Ni_{30}Al_5Ti_5$ MPEA was developed by Al/Ti alloying of CrFeNi. The as-cast alloy contains an FCC/BCC-based heterogeneous structure with coherent $L1_2$ precipitates in the FCC matrix and hierarchical $L2_1$, B2, and η-Ni_3Ti-related ordered precipitates in the BCC regions, and exhibits an excellent strength-ductility combination [25]. Building on this alloy system, the present study examines three representative microstructural states: as-cast equiatomic CrFeNi (denoted as AC-CrFeNi), as-cast $Cr_{30}Fe_{30}Ni_{30}Al_5Ti_5$ (AC-CrFeNiAlTi), and hot-rolled $Cr_{30}Fe_{30}Ni_{30}Al_5Ti_5$ (HR-CrFeNiAlTi). This design enables the corrosion response to be evaluated through two successive comparisons. The comparison between AC-CrFeNi and AC-CrFeNiAlTi reveals how Al/Ti addition, together with the associated transition from a single-phase FCC structure to a chemically partitioned FCC/BCC multiphase microstructure, affects the electrochemical behavior. The comparison between AC-CrFeNiAlTi and HR-CrFeNiAlTi then highlights the effects associated with processing-induced microstructural reorganization more clearly, because the nominal alloy composition remains unchanged while the FCC/BCC regions evolve from a relatively equiaxed as-cast morphology into a directional

lamellar arrangement. This sequential comparison therefore provides a basis for distinguishing the effects of phase constitution and chemical partitioning from those associated with phase morphology and spatial organization.

Accordingly, this study investigates AC-CrFeNi, AC-CrFeNiAlTi, and HR-CrFeNiAlTi in 3.5 wt.% NaCl solution using potentiodynamic polarization, electrochemical impedance spectroscopy (EIS), equivalent-circuit analysis, and post-electrochemical scanning electron microscopy/energy-dispersive X-ray spectroscopy (SEM/EDS) and X-ray diffraction (XRD). The analysis is organized around two questions: how Al/Ti-induced phase heterogeneity changes the overall electrochemical response relative to single-phase CrFeNi, and how subsequent reorganization of the same CrFeNiAlTi composition into a lamellar morphology changes impedance, interfacial relaxation, and the spatial distribution of localized attack. By using these two comparisons, the work aims to assess the roles of phase constitution and processing-related microstructural organization in chloride corrosion of CrFeNi-based MPEAs.

2. Materials and Methods

2.1. Alloy Preparation and Hot Rolling

The nominal compositions of the investigated materials were equiatomic CrFeNi and $Cr_{30}Fe_{30}Ni_{30}Al_5Ti_5$ (at.%). Both alloys were prepared by vacuum arc melting from high-purity elemental feedstock (≥99.9 wt.%) under a high-purity Ar atmosphere. Each ingot was flipped and remelted at least five times to improve chemical homogeneity, followed by suction casting into a water-cooled Cu mold to produce plates of approximately 40 mm × 10 mm × 10 mm. The as-cast equiatomic CrFeNi and $Cr_{30}Fe_{30}Ni_{30}Al_5Ti_5$ alloys are denoted as AC-CrFeNi and AC-CrFeNiAlTi, respectively. The preparation route and basic phase constitution of the as-cast CrFeNiAlTi alloy were systematically reported in our previous work [25]. HR-CrFeNiAlTi was produced using a multi-pass hot-rolling route. The as-cast $Cr_{30}Fe_{30}Ni_{30}Al_5Ti_5$ alloy was first homogenized at 1423 K for 24 h and then hot rolled at 1423 K in three passes. After each pass, the sample was reheated and held at 1423 K for 10 min before the subsequent pass. The final total thickness reduction was approximately 80%. No post-rolling annealing treatment was applied to the HR material examined in this study.

2.2. Microstructural and Post-Electrochemical Surface Characterization

Phase constitution was examined by X-ray diffraction (XRD, Rigaku D/max-rB) using Cu Kα radiation at 40 kV and 40 mA. Patterns were recorded from 20° to 80° in 2θ at a nominal scan rate of 6° min^{-1} with a recorded step interval of 0.02°. Microstructure and elemental distributions were characterized by scanning electron microscopy (SEM; ZEISS Sigma 500, Carl Zeiss Microscopy GmbH, Jena, Germany) equipped with energy-dispersive X-ray spectroscopy (EDS; Oxford Aztec X-MAX50, Oxford Instruments plc, Abingdon, UK). The working surfaces were prepared by successive SiC-paper grinding and diamond polishing. Following electrochemical testing, the exposed electrode surfaces were used for SEM/EDS observations and XRD measurements of corrosion morphology, elemental distributions, and retained crystalline phases.

2.3. Electrochemical Measurements and Area Normalization

Electrochemical specimens, approximately 10 mm × 10 mm × 2 mm, were sectioned from the alloy plates, electrically connected to Cu wires, and mounted in epoxy resin with one working surface exposed. The exposed surfaces were sequentially ground using 180, 400, 800, 1200, 1500, 2000, 2500, and 3000 grit SiC papers and then polished using 3 μm and 1 μm diamond suspensions. Electrochemical measurements were performed in a conventional three-electrode cell using and CHI760E electrochemical workstations (Shanghai Chenhua Instrument Co., Ltd., Shanghai, China), with the alloy specimen as the working electrode, a Pt plate as the counter electrode, and a saturated calomel electrode (SCE) as the reference electrode. The electrolyte was an aqueous 3.5 wt.% NaCl solution at room temperature.

After immersion, the open-circuit potential (OCP) was monitored until a relatively stable value was reached, after which EIS was performed. EIS measurements were conducted over 100 kHz–0.01 Hz using a sinusoidal perturbation amplitude of 5 mV. Potentiodynamic polarization was conducted from negative to positive potential using an instrument-programmed range of −2 to +2 V vs. SCE at a scan rate of 3 mV s^{-1}. Because the current approached the instrumental current-range limit at high anodic polarization, the extreme-potential region was not used to determine a common passive current density or pitting potential. Tafel parameters were obtained from the corrosion-potential region unaffected by current limiting, following the conventional polarization-analysis framework [26].

Because the actual exposed areas of the epoxy-mounted electrodes were not identical, both current and impedance were normalized using the measured exposed area:

$$j = I/A \tag{1}$$

$$Z_A = Z \times A \tag{2}$$

where j is the current density, I is the measured current, A is the actual exposed area, and Z_A is the area-normalized impedance. Potentiodynamic polarization curves and Tafel parameters were obtained from area-normalized current densities. Nyquist and Bode impedance data were likewise normalized using the actual exposed area of the corresponding electrode.

2.4. Equivalent-Circuit Fitting of EIS Data

The EIS spectra were fitted by complex nonlinear least-squares analysis. A constant phase element (CPE) was used to represent non-ideal capacitive behavior, with $Z_{CPE} = [Q(j\omega)^n]^{-1}$, where Q is the CPE coefficient, ω is the angular frequency, j is the imaginary unit, and n ($0 < n \leq 1$) describes the deviation from ideal capacitive behavior. The use and interpretation of CPEs for heterogeneous electrochemical interfaces are well established [27,28]. Based on the resolvable relaxation features in the Nyquist and Bode spectra, AC-CrFeNi and AC-CrFeNiAlTi were fitted using R_s-(R_1 ‖ CPE_1)-(R_2 ‖ CPE_2), whereas HR-CrFeNiAlTi was fitted using R_s-(R_{ct} ‖ CPE_{dl}). The sensitivity of the HR-CrFeNiAlTi fit to model selection was evaluated by re-fitting its original complex-impedance data with both one- and two-time-constant circuits over 0.01–99,950 Hz. The model comparison used inverse-impedance-modulus weighting on the real and imaginary components, multistart optimization, residual inspection, and tests of parameter plausibility and frequency-window sensitivity (Supplementary Materials Table S1 and Figure S1).

3. Results and Discussion

3.1. Microstructural Characteristics

The as-cast microstructures of AC-CrFeNi and AC-CrFeNiAlTi were systematically characterized in our previous work and are therefore only summarized here. AC-CrFeNi is dominated by a single FCC phase [25]. After the addition of 5 at. % Al and 5 at. % Ti, AC-CrFeNiAlTi develops an FCC/BCC dual-phase microstructure containing approximately 53 vol.% FCC and 47 vol.% BCC regions, together with multiscale ordered precipitates. Previous TEM characterization further identified coherent $L1_2$ nanoprecipitates in the FCC matrix and $L2_1$, B2, and η-Ni_3Ti-related ordered structures within the BCC regions.

Figure 1 shows the representative microstructure of HR-CrFeNiAlTi. As shown in Figure 1a, in contrast to AC-CrFeNiAlTi, where relatively equiaxed BCC regions are dispersed within a continuous FCC framework, the two constituent regions are markedly elongated along the rolling direction in the hot rolling condition, producing a directional lamellar dual-phase morphology. The initially more equiaxed phase regions are stretched and rearranged, resulting in alternating FCC- and BCC-rich bands along the rolling direction. Higher-magnification SEM observations reveal a clear microstructural contrast between the phase regions in the hot rolling condition (Figure 1b). Numerous fine precipitates remain visible within the BCC-rich regions, while some coarser particles occur near BCC-region boundaries. According to the TEM and electron-diffraction results previously obtained for the same $Cr_{30}Fe_{30}Ni_{30}Al_5Ti_5$ alloy, the as-cast BCC regions contain $L2_1$-, B2-, and η-related ordered structures, whereas the FCC matrix contains $L1_2$ nanoprecipitates [25]. Accordingly, the fine particles observed by SEM in the hot rolling state are treated as retained precipitation features. Overall, the hot rolling condition retains the basic FCC/BCC dual-phase character of $Cr_{30}Fe_{30}Ni_{30}Al_5Ti_5$ but exhibits a pronounced transformation from the relatively equiaxed as-cast phase morphology to a lamellar arrangement aligned with the rolling direction. A clear processing-related difference between AC-CrFeNiAlTi and HR-CrFeNiAlTi is therefore the morphology and spatial distribution of the FCC/BCC regions. Image-Pro analysis of the HR-CrFeNiAlTi micrographs yielded FCC and BCC area fractions of approximately 72.61% and 27.39%, respectively. Compared with the previously reported as-cast phase fractions of approximately 53 vol.% FCC and 47 vol.% BCC [25], these results indicate a change in the apparent phase balance after homogenization and hot rolling, together with the formation of the directional lamellar morphology.

3.2. Potentiodynamic Polarization Behavior

Figure 2 compares the potentiodynamic polarization curves of AC-CrFeNi, AC-CrFeNiAlTi, and HR-CrFeNiAlTi in 3.5 wt.% NaCl. The corresponding corrosion potentials (E_{corr}) are approximately −0.8299, −0.8892,

and −0.8721 V vs. SCE, respectively. AC-CrFeNi shows the most positive E_{corr}, whereas AC-CrFeNiAlTi and HR-CrFeNiAlTi shift toward more negative potentials. This sequence does not follow the variation in corrosion current density. Because E_{corr} is a mixed potential established by the balance of anodic and cathodic partial reactions, it is not a direct measure of corrosion rate; the near-corrosion-potential reaction kinetics are compared using corrosion current density (i_{corr}), together with independent EIS results [26]. Tafel extrapolation gives icorr values of 15.15, 9.302, and 6.47 μA cm^{-2} for AC-CrFeNi, AC-CrFeNiAlTi, and HR-CrFeNiAlTi, respectively. The transition from AC-CrFeNi to AC-CrFeNiAlTi decreases i_{corr} by ~38.6%. At the same nominal CrFeNiAlTi composition, the HR condition shows a further decrease of approximately 30.4%, giving an overall reduction of approximately 57.3% relative to AC-CrFeNi. Thus, the polarization data indicate a monotonic decrease in the estimated near-corrosion-potential reaction kinetics across AC-CrFeNi, AC-CrFeNiAlTi, and HR-CrFeNiAlTi under the present test conditions. The anodic branches show the same qualitative tendency. Above E_{corr}, AC-CrFeNi exhibits the most rapid increase in anodic current, AC-CrFeNiAlTi maintains a lower current density over the corresponding potential range, and HR-CrFeNiAlTi shows the lowest anodic current level. None of the three curves exhibits a broad, stable passive plateau that can be defined consistently using a common criterion. Accordingly, a common passive current density (i_{pass}) or pitting potential (E_{pit}) is not extracted, and i_{corr} is used only as an estimate of the area-averaged corrosion kinetics near E_{corr}, not as a measure of passive-film stability or the complete anodic response. The electrochemical ranking is independently examined using the low-frequency EIS data in Section 3.3.

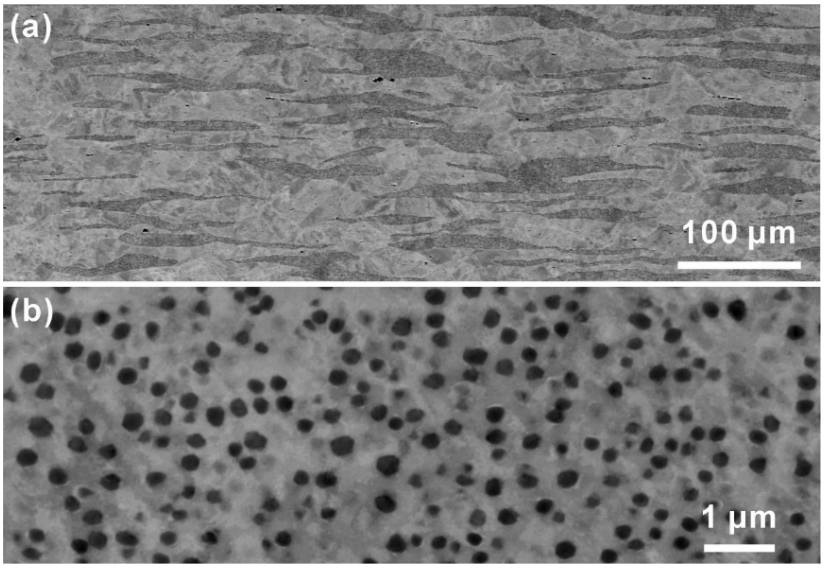

Figure 1. Microstructural characteristics of HR-CrFeNiAlTi: (**a**) low-magnification SEM image showing the elongated lamellar morphology; (**b**) high-magnification SEM image of a precipitate-containing BCC-rich region.

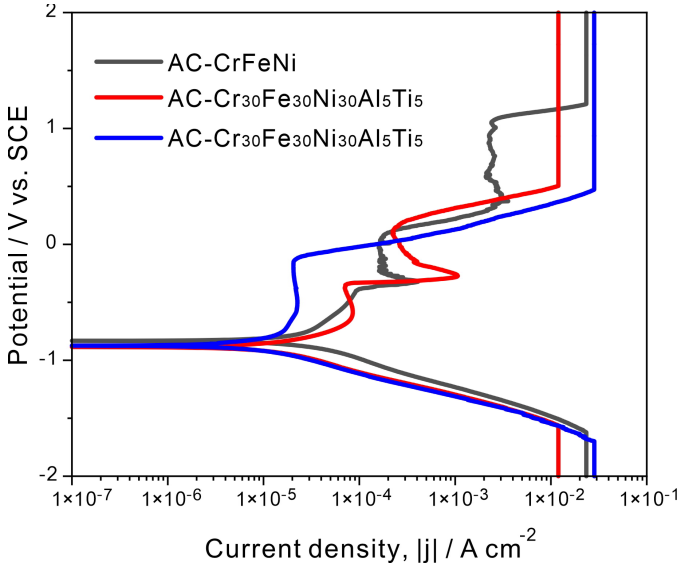

Figure 2. Potentiodynamic polarization curves of AC-CrFeNi, AC-CrFeNiAlTi, and HR-CrFeNiAlTi in 3.5 wt.% NaCl.

3.3. Electrochemical Impedance Response and Equivalent-Circuit Analysis

Figure 3 presents the Nyquist and Bode spectra of AC-CrFeNi, AC-CrFeNiAlTi, and HR-CrFeNiAlTi in 3.5 wt.% NaCl. All three states exhibit non-ideal capacitive behavior, but their impedance levels differ substantially. In Figure 3a, AC-CrFeNi shows the smallest depressed capacitive arc, AC-CrFeNiAlTi exhibits a larger arc, and HR-CrFeNiAlTi extends to the highest real and imaginary impedance over the measured frequency window. The impedance response therefore follows the order HR-CrFeNiAlTi > AC-CrFeNiAlTi > AC-CrFeNi. The use of Nyquist/Bode response and low-frequency impedance to compare corrosion resistance is well established across Cr/Fe/Ni- and Co/Cr/Ni-based MPEA [17,29,30]. The same trend is resolved more clearly in the Bode impedance-modulus plots (Figure 3b). The three states differ only slightly at high frequency, whereas their impedance moduli separate progressively toward low frequency. At 0.01 Hz, the area-normalized |Z| values are 9.457, 16.702, and 47.176 kΩ cm^2 for AC-CrFeNi, AC-CrFeNiAlTi, and HR-CrFeNiAlTi, respectively. AC-CrFeNiAlTi therefore exhibits a low-frequency impedance approximately 1.77 times that of AC-CrFeNi. In the HR condition, $|Z|_{0.01\ \mathrm{Hz}}$ increases to approximately 2.82 times that of AC-CrFeNiAlTi and 4.99 times that of AC-CrFeNi. This progressive increase in low-frequency impedance is consistent with the decrease in i_{corr} obtained from the polarization measurements. The Bode phase-angle spectra further differentiate the interfacial relaxation behavior (Figure 3c). AC-CrFeNi and AC-CrFeNiAlTi exhibit maximum phase angles of approximately 74.5° and 75.6° at 26.1 and 21.54 Hz, respectively. By contrast, HR-CrFeNiAlTi reaches approximately 82.2°, and the phase-angle maximum shifts to approximately 1.212 Hz. The higher and broader phase-angle response indicates a more pronounced capacitive contribution in the HR state, while the shift toward lower frequency reflects a longer characteristic time scale for the dominant interfacial relaxation process. Distributed relaxation of this type is commonly represented using CPE-based impedance models [27,28].

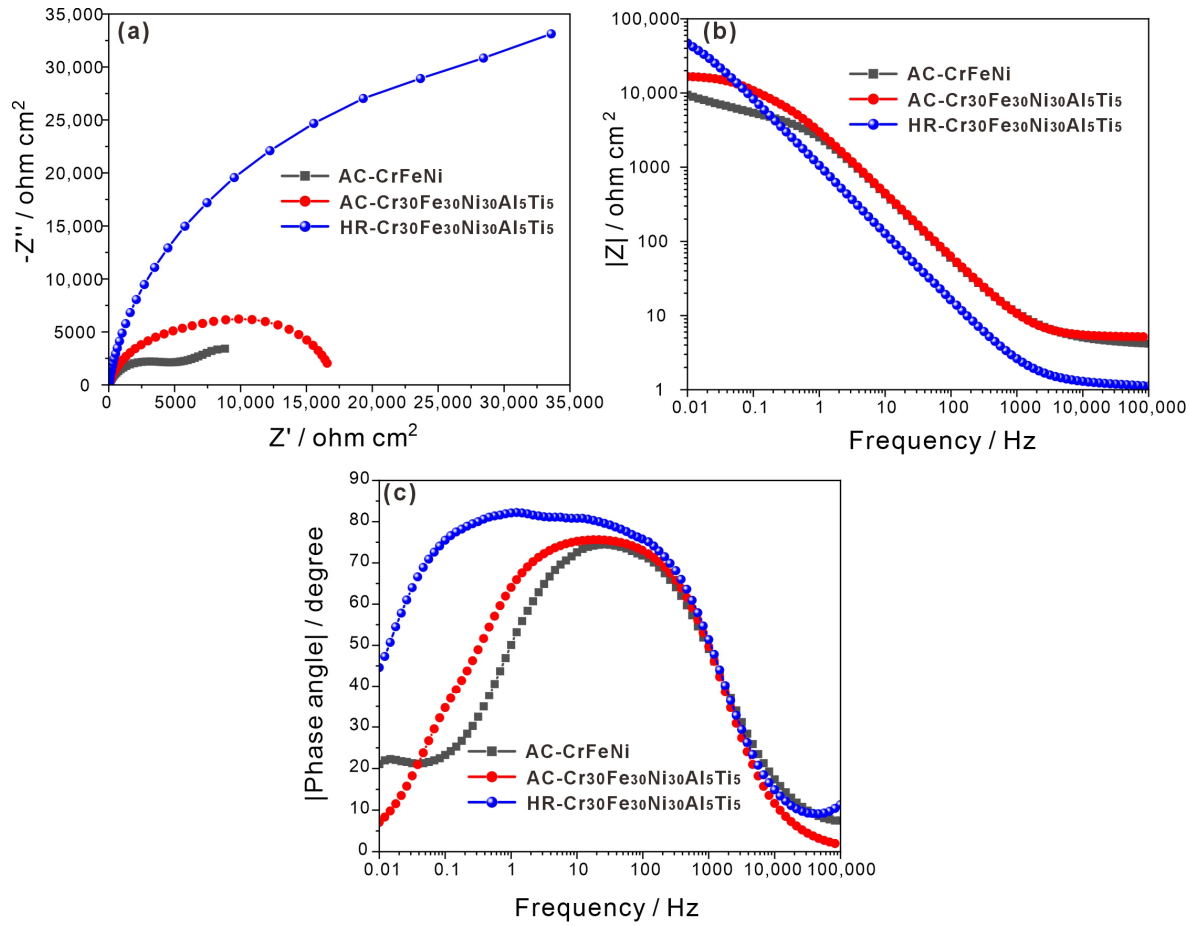

Figure 3. Experimental and fitted EIS spectra of AC-CrFeNi, AC-CrFeNiAlTi, and HR-CrFeNiAlTi in 3.5 wt.% NaCl: (**a**) Nyquist plots; (**b**) Bode impedance-modulus plots; and (**c**) Bode phase-angle plots.

To quantify these impedance responses, the spectra were fitted using the equivalent circuits shown in Figure 4. A CPE was used to describe the non-ideal capacitive response of the heterogeneous electrode interfaces, with $Z_{CPE} = [Q(j\omega)^n]^{-1}$. Here, Q is the CPE coefficient, ω is the angular frequency, j is the imaginary unit, and n is the CPE exponent; n approaching 1 corresponds to increasingly ideal capacitive behavior [27,28]. AC-CrFeNi and

AC-CrFeNiAlTi were described using the two-time-constant model R_s-(R_1 ∥ CPE_1)-(R_2 ∥ CPE_2), where R_s is the solution resistance and the R_1/CPE_1 and R_2/CPE_2 branches phenomenologically represent the two resolvable interfacial relaxation processes. HR-CrFeNiAlTi was fitted using the simpler one-time-constant model R_s-(R_{ct} ∥ CPE_{dl}), in which R_{ct} is the low-frequency interfacial resistance parameter of the model. The use of different minimum circuits is consistent with the number of relaxation features resolved in the corresponding Nyquist and Bode spectra. The HR spectrum was also tested using the two-time-constant circuit as a model-sensitivity check (Supplementary Materials Table S1 and Figure S1).

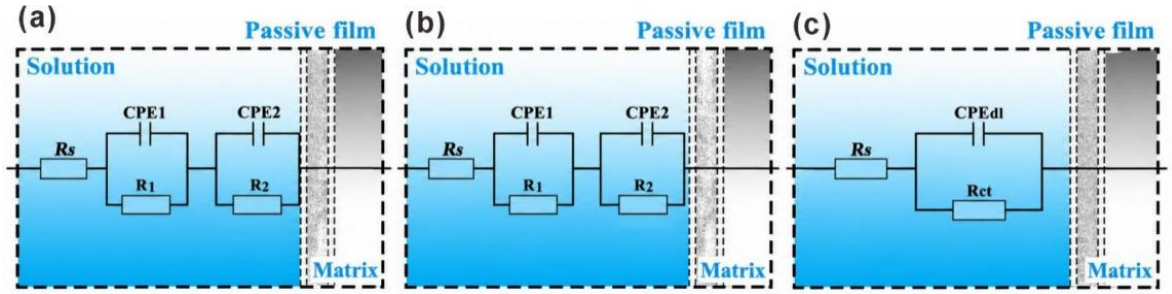

Figure 4. Equivalent circuits used to fit the representative EIS spectra: (**a**) AC-CrFeNi; (**b**) AC-CrFeNiAlTi; and (**c**) HR-CrFeNiAlTi. CPE denotes a constant phase element; for the HR model, $R_p = R_{ct}$.

For AC-CrFeNi, R_s is approximately 4.20 Ω cm^2, while R_1 and R_2 are approximately 3.81 and 10.68 kΩ cm^2, giving an effective polarization resistance $R_p = R_1 + R_2$ of approximately 14.49 kΩ cm^2. For AC-CrFeNiAlTi, R_1 and R_2 are approximately 8.28 and 8.75 kΩ cm^2, respectively, and R_p increases to approximately 17.03 kΩ cm^2, about 17.5% above that of AC-CrFeNi. The fitted response of the two as-cast states is consistent with the experimental increase in $|Z|_{0.01\ Hz}$ from 9.457 to 16.702 kΩ cm^2. For HR-CrFeNiAlTi, the one-time-constant fit gives $R_{ct} \approx 75.41$ kΩ cm^2, approximately 4.43 and 5.20 times the fitted R_p values of AC-CrFeNiAlTi and AC-CrFeNi, respectively, with $n \approx 0.902$. A re-fit of the original HR impedance data reproduced $R_{ct} = 75.414$ kΩ cm^2. A two-time-constant model lowered the weighted residual sum of squares from 0.2516 to 0.0251 and yielded a total resistance $R_1 + R_2 \approx 73.312$ kΩ cm^2 (2.8% below the single-time-constant estimate). However, the additional branch contributed only approximately 1.50 Ω cm^2 and had a fitted characteristic frequency of approximately 2.43 MHz, well above the experimental upper frequency limit. The unconstrained two-time-constant fit also drove the solution resistance toward zero. Furthermore, the parameters assigned to the additional branch varied substantially when the high-frequency fitting limit was changed (Table S1). The comparison between alloy states is thus based primarily on the measured |Z| at 0.01 Hz and the independent polarization results, rather than on differences between fitted resistances obtained using dissimilar equivalent circuits.

3.4. Post-Electrochemical Localized Corrosion Characteristics

Figure 5 shows the post-electrochemical surface morphology and EDS elemental distributions of AC-CrFeNi. Figure 5b is an enlarged view of the yellow solid line frame in Figure 5a, and Figure 5c is an enlarged view of the yellow dotted rectangle in Figure 5b. Discrete locally attacked regions are distributed over the surface, and some exhibit pronounced pit-like or groove-like morphologies. The attack is spatially non-uniform and is concentrated near selected as-cast microstructural boundaries or cellular features, demonstrating a clear localized-corrosion character under the present test conditions. This behavior is consistent with recent work on Cr-containing MPEAs showing that apparently modest local heterogeneities, including minor alloying-induced segregation, inclusions, and processing-derived structural discontinuities, can determine where chloride attack initiates even when the bulk electrochemical response is governed by the surrounding matrix [31–36].

Figure 5d–g present EDS elemental maps corresponding to the region shown in Figure 5c. The corresponding EDS maps show a pronounced enhancement of the O signal within the attacked regions, while Cr, Fe, and Ni retain the overall distribution of the metallic matrix. The O enrichment is consistent with local accumulation of oxygen-containing corrosion products after electrochemical testing. Surface-sensitive studies on related MPEAs show that passive layers commonly contain spatially and chemically heterogeneous oxide/hydroxide species whose protectiveness depends on alloy chemistry and local partitioning [37–39]. The present EDS result is therefore used as evidence of oxygen-containing corrosion products.

The FCC-rich and BCC-rich labels in Figure 6 were assigned from the phase-morphology correspondence previously established for this $Cr_{30}Fe_{30}Ni_{30}Al_5Ti_5$ alloy by EBSD/TEM characterization [25], together with the characteristic elemental distributions observed by EDS (Figure 7). Compared with single-phase AC-CrFeNi, AC-

CrFeNiAlTi shows a clearer correspondence between localized attack and the FCC/BCC dual-phase microstructure (Figure 6). Localized corrosion is observed in regions associated with both FCC-rich and BCC-rich constituents, while selected regions adjacent to the two constituents exhibit more pronounced surface damage. Comparable phase-selective behavior has been resolved more directly in other Al-containing multiphase alloys. In an $L2_1$-strengthened $(CoCrFeNi)_{86}Al_7Ti_7$ alloy, the FCC and $L2_1$ phases developed different passive films and a micro-galvanic couple that promoted pitting at the two-phase interface [40]. Preferential attack of ordered Al/Ni-rich regions has also been reported in FCC+B2/BCC $AlCrFeNi_3Cu_x$ alloys and $AlCoCrFeNi_{2.1}$ eutectic alloys [41,42]. These studies provide a mechanistic framework for interpreting the stronger spatial dependence observed here.

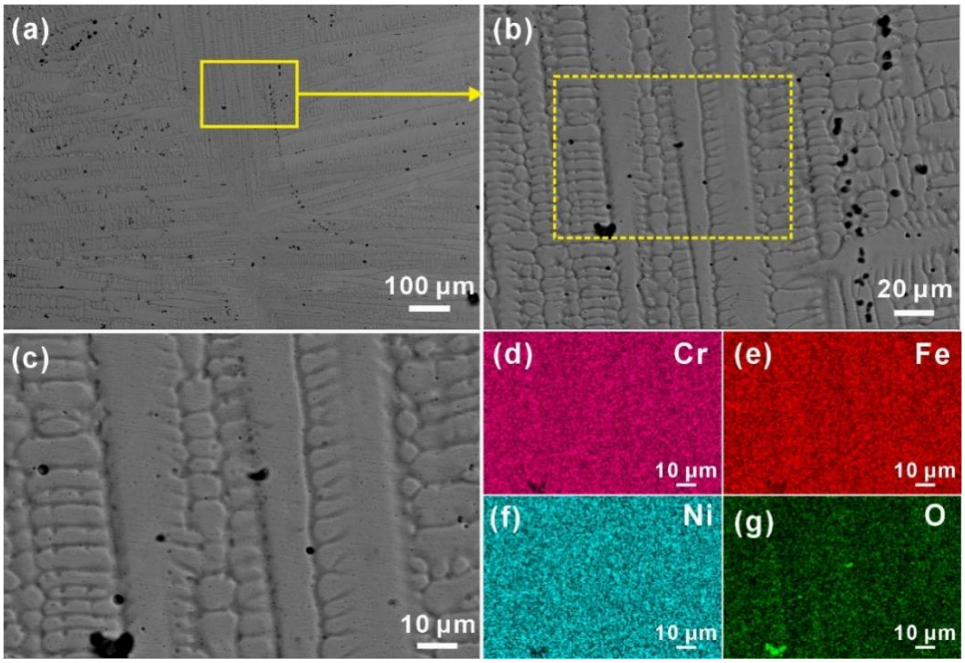

Figure 5. Post-electrochemical corrosion morphology and elemental distributions of AC-CrFeNi after testing in 3.5 wt.% NaCl: (**a**) low-magnification SEM image; (**b**) enlarged view of the region marked in (**a**); (**c**) further enlargement of the dotted yellow rectangle in (**b**); and (**d**–**g**) corresponding EDS maps of Cr, Fe, Ni, and O.

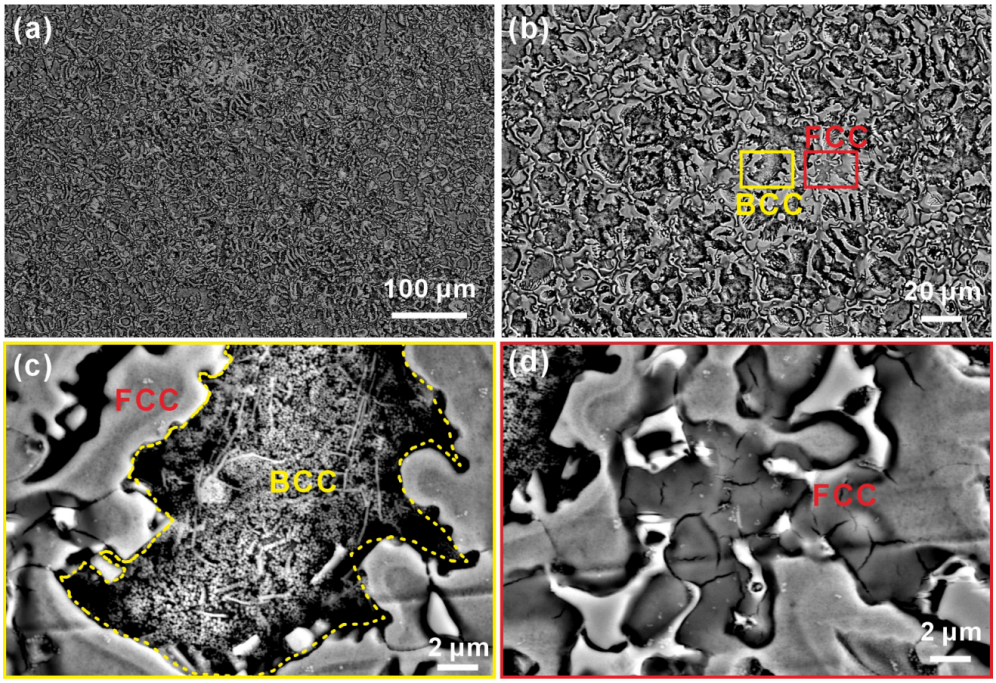

Figure 6. Post-electrochemical SEM morphologies of AC-CrFeNiAlTi: (**a**) low-magnification overview; (**b**) enlarged view showing the selected FCC-rich and BCC-rich regions; (**c**) higher-magnification view of a locally attacked BCC-rich region and its adjacent FCC-rich region; and (**d**) higher-magnification view of a locally attacked FCC-rich region.

The EDS maps in Figure 7 show clear O enrichment in locally attacked regions, while Cr, Fe, Ni, Al, and Ti retain heterogeneous distributions corresponding to the FCC/BCC phase regions. Together with the previously established phase constitution and phase chemistry [25], these observations indicate that localized corrosion in AC-CrFeNiAlTi is coupled to the spatial distribution of the constituent phase regions and their adjacent areas. This interpretation is consistent with studies of Cr-Fe-Ni-Nb eutectic alloys, $L2_1$-strengthened Al/Ti-containing alloys, and FCC+B2/BCC eutectic systems, in which phase partitioning and interphase electrochemical contrast redistribute pitting or selective dissolution [19,20,40–42]. The important point for the present alloy is therefore not that multiphase character necessarily lowers corrosion resistance, but that it makes the location of attack more microstructure-dependent.

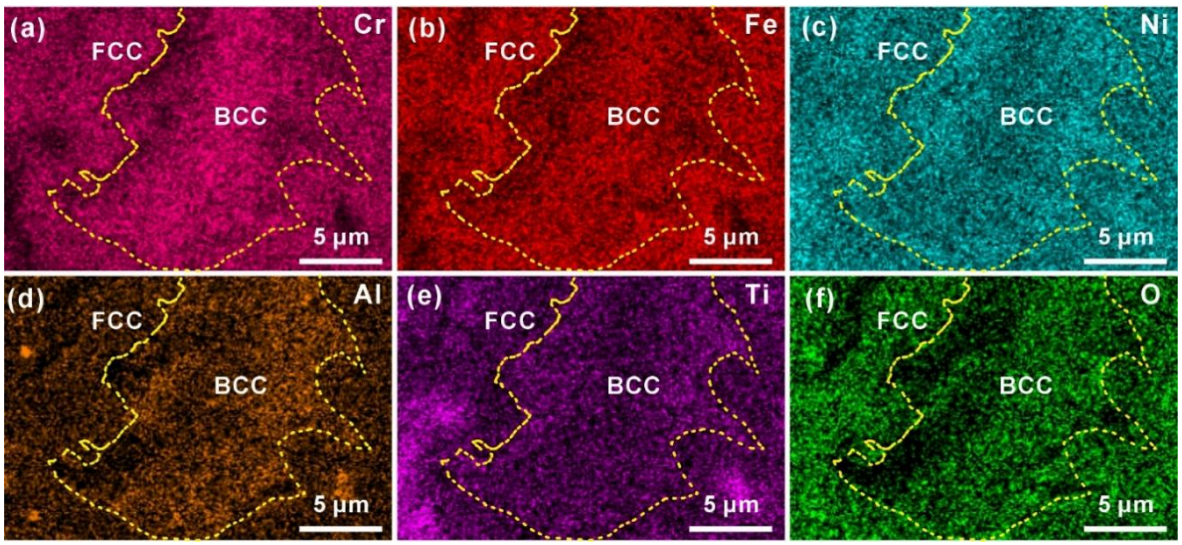

Figure 7. EDS elemental maps of a representative locally attacked region in AC-CrFeNiAlTi after electrochemical testing: (**a**) Cr; (**b**) Fe; (**c**) Ni; (**d**) Al; (**e**) Ti; and (**f**) O.

After electrochemical testing, the lamellar morphology aligned with the rolling direction remains recognizable in HR-CrFeNiAlTi (Figure 8). Localized attack shows a directional distribution along the rolled phase regions, with more evident surface damage in selected regions and adjacent areas. The EDS maps in Figure 9 likewise show enhanced O signals at the more strongly attacked locations, whereas the distributions of Cr, Fe, Ni, Al, and Ti remain correlated with the lamellar microstructure. This directional correspondence is important because recent studies distinguish phase fraction from phase morphology: FCC/BCC morphology and passive-film defects can change together even at comparable phase fractions [21], while deliberately constructed heterogeneous lamellar structures can redirect localized attack along their constituent regions [22]. Thermomechanical processing, grain-boundary engineering, and annealing studies further show that corrosion is sensitive to the spatial rearrangement of phases and interfaces produced during processing [23,24,43,44]. The present HR state follows the same general principle, but its interpretation is anchored by the direct comparison with the same nominal CrFeNiAlTi composition in the as-cast state.

To examine the crystalline structures retained after the electrochemical tests, XRD was performed on the exposed surfaces of all three materials (Figure 10). The post-test diffraction pattern of AC-CrFeNi remains dominated by FCC reflections, with peaks near 43.7°, 50.8°, and 74.7° assigned to FCC (111), FCC (200), and FCC (220), respectively. Compared with the pre-test XRD pattern, AC-CrFeNi retains its primary FCC structure after electrochemical testing. AC-CrFeNiAlTi likewise retains both FCC and BCC reflections after electrochemical testing. The principal peaks at approximately 43.42°, 44.62°, 50.58°, 64.94°, and 74.28° correspond to FCC (111), BCC (110), FCC (200), BCC (200), and FCC (220), respectively. Their positions remain close to those in the as-cast alloy before electrochemical testing, showing that the FCC/BCC matrix structure is retained. HR-CrFeNiAlTi also retains the principal FCC/BCC diffraction features after electrochemical testing, together with weak reflections near 30.5° and 63° that are consistent with B2/$L2_1$-related ordered structures previously identified in this alloy [25].

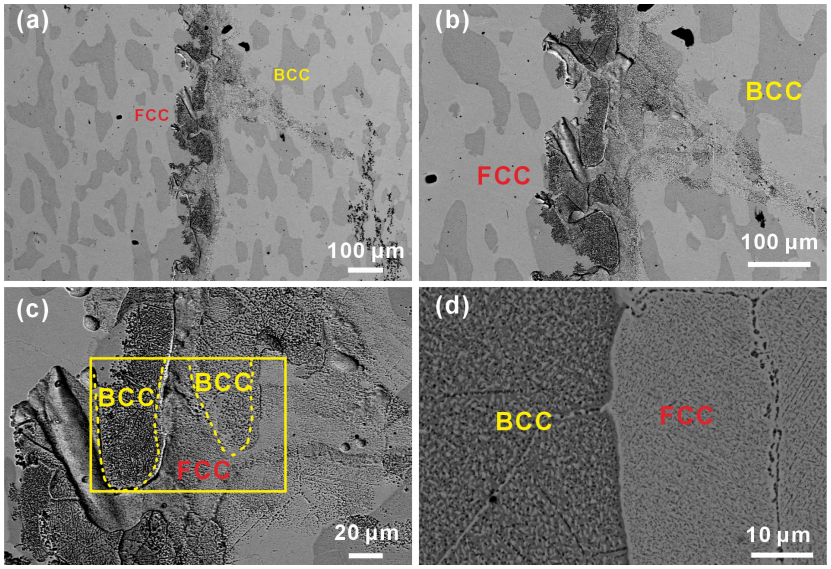

Figure 8. Localized corrosion morphologies of HR-CrFeNiAlTi after electrochemical testing in 3.5 wt.% NaCl: (**a**) surface overview; (**b**) enlarged area showing FCC-rich and BCC-rich regions and localized attack; (**c**) enlarged interfacial region with the area selected for EDS mapping indicated by the yellow rectangle; and (**d**) higher-magnification view of an FCC/BCC-adjacent region.

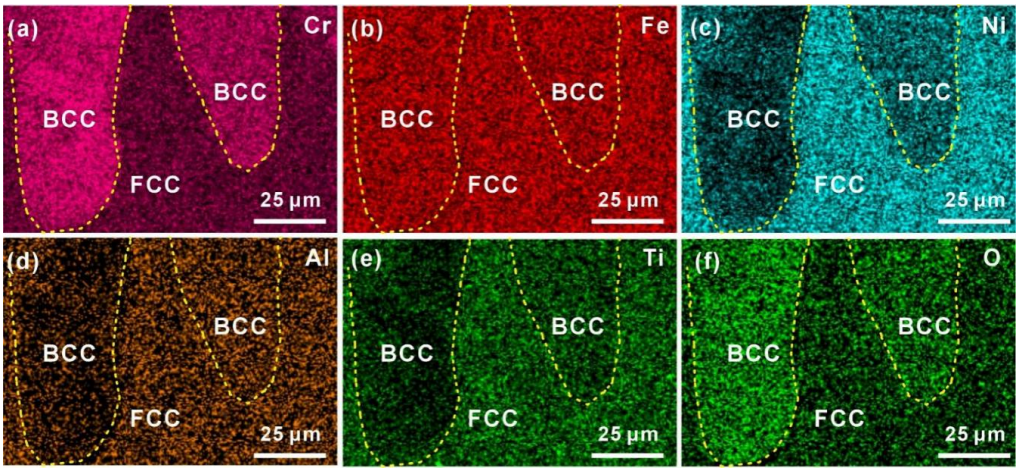

Figure 9. EDS elemental maps of a representative locally corroded region in HR-CrFeNiAlTi after electrochemical testing: (**a**) Cr; (**b**) Fe; (**c**) Ni; (**d**) Al; (**e**) Ti; and (**f**) O. The EDS area within the yellow box in Figure 8c.

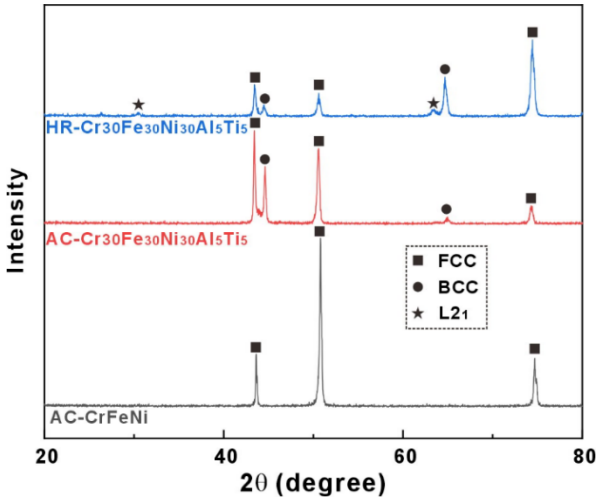

Figure 10. XRD patterns of AC-CrFeNi, AC-CrFeNiAlTi, and HR-CrFeNiAlTi after completion of the electrochemical testing sequence in 3.5 wt.% NaCl.

3.5. Corrosion Mechanism

The corrosion response of the present alloys can be rationalized through a hierarchical mechanism linking phase chemistry, local electrochemical heterogeneity, interfacial electrochemical response, localized attack, and finally the spatial morphology of the constituent phases. These levels should not be treated independently. Phase constitution and elemental partitioning define chemically distinct surface regions; those regions can develop different interfacial electrochemical responses when exposed to chloride solution; such local differences may influence the sites at which corrosion initiates; and the morphology and connectivity of the heterogeneous regions control how such local processes are spatially coupled over the macroscopic electrode. This framework also explains why the area-averaged electrochemical ranking and the local corrosion morphology need not vary in the same manner: across AC-CrFeNi, AC-CrFeNiAlTi, and HR-CrFeNiAlTi, i_corr decreases and $|Z|_{0.01}$ Hz increases, yet localized attack remains detectable in all three states.

The first level is phase chemistry. AC-CrFeNi provides a predominantly single-FCC reference, whereas Al/Ti addition produces an FCC/BCC microstructure containing $L1_2$, $L2_1$, B2, and η-Ni_3Ti-related ordered precipitates [25]. This change necessarily redistributes Cr, Fe, Ni, Al, and Ti among different local environments and therefore creates chemically nonequivalent electrochemical regions. Importantly, the corrosion consequence of such heterogeneity is not intrinsically beneficial or detrimental. In $(CoCrFeNi)_{86}Al_7Ti_7$, the passive film on the FCC phase was reported to be more protective than that on the $L2_1$ phase, and FCC/$L2_1$ micro-galvanic coupling promoted pitting initiation at the two-phase interface [40]. Al–Ni-rich regions in $AlCoCrFeNi_{2.1}$ have likewise been identified as preferential dissolution sites in chloride solution [42]. By contrast, coherent nanoprecipitates with small compositional and structural contrast can improve pitting resistance by favorably modifying the passive-film chemistry [45], while appropriate aging of $(FeCoNi)_{86}Al_7Ti_7$ can optimize compositional homogeneity and passive-film quality [13,14]. These comparisons show that phase chemistry, compositional contrast, and phase-specific surface-film response are more fundamental than the simple presence of a second phase.

The second level is the local electrochemical heterogeneity generated by this phase chemistry. In AC-CrFeNiAlTi, i_{corr} decreases from 15.15 to 9.302 μA cm^{-2} and $|Z|_{0.01}$ Hz increases from 9.457 to 16.702 kΩ cm^2 relative to AC-CrFeNi, indicating slower area-averaged electrochemical kinetics. At the same time, post-electrochemical SEM/EDS reveals that corrosion remains spatially non-uniform and is associated with the FCC/BCC regions and selected adjacent areas. The coexistence of improved global impedance with locally selective attack is therefore not contradictory. Rather, it indicates that the Al/Ti-induced multiphase state reduces the net electrochemical reaction rate of the exposed surface while introducing local differences in electrochemical susceptibility.

The third level is the interfacial relaxation response. The EIS spectra of AC-CrFeNi and AC-CrFeNiAlTi were fitted using two-time-constant models, whereas a single dominant CPE-based circuit was retained as a parsimonious representation of the HR-CrFeNiAlTi response. A two-time-constant alternative reduced the residuals but introduced a small high-frequency branch with unstable or boundary-limited parameters, and no independent additional process could be assigned reliably within the measured range (Table S1 and Fig. S1). More importantly, HR-CrFeNiAlTi exhibits the highest $|Z|_{0.01}$ Hz (47.176 kΩ cm^2), the largest maximum phase angle (82.2°), and a marked shift of the phase-angle maximum from 21.54 Hz in AC-CrFeNiAlTi to 1.212 Hz. The increased impedance and more nearly capacitive phase-angle response are consistent with greater impedance to the collective interfacial electrochemical response, while the shift toward lower frequency reflects a substantially longer dominant relaxation time scale. These observations show that the HR state has a different, more nearly capacitive collective electrode/electrolyte response.

The fourth level is localized corrosion. Chloride ions can exploit the least stable parts of a chemically heterogeneous interface, so local breakdown can occur even when the macroscopic electrode exhibits relatively high impedance. Post-electrochemical XRD confirmed that AC-CrFeNi retained its primary FCC structure, whereas both AC-CrFeNiAlTi and HR-CrFeNiAlTi retained their FCC/BCC structures. The most defensible interpretation is therefore localized surface oxidation/corrosion-product accumulation on an otherwise retained metallic matrix. This observation is compatible with the phase-selective corrosion reported for $L2_1$-strengthened and eutectic HEAs, where local passive-film differences and micro-galvanic effects promote preferential attack of specific phase regions or phase boundaries [40–42].

The fifth level is the lamellar morphology effect. AC-CrFeNiAlTi and HR-CrFeNiAlTi have the same nominal composition, but rolling reorganizes the relatively equiaxed FCC/BCC regions into an elongated directional morphology. This composition-controlled comparison highlights processing-related spatial reorganization, but it does not isolate phase morphology as the only variable: Image-Pro measurements show FCC and BCC area fractions of ~72.6% and ~27.4% in the HR state, compared with previously reported as-cast phase fractions of ~53 vol.% FCC and ~47 vol.% BCC. Thus, phase balance changes along with morphology, while

rolling may also affect defect density, grain structure, residual stress, and precipitation. The HR material exhibits the lowest i_{corr} (6.47 μA cm^{-2}) and the highest low-frequency impedance, while its post-test corrosion morphology follows the directional phase arrangement. Recent studies provide a consistent mechanistic precedent: the corrosion response of $Al_xFeNiCrCo$ alloys was shown to depend jointly on FCC/BCC morphology and passive-film defect structure [21], and a multi-level heterogeneous lamellar eutectic alloy displayed substantially improved corrosion resistance after heterostructure construction in association with altered film characteristics [22]. For the present alloy, morphology is considered one potential contributor because it changes the geometry, continuity, interfacial density, and spatial coupling of chemically distinct regions, rather than because a lamellar structure itself acts as a simple physical barrier to corrosion.

Accordingly, the corrosion mechanism proposed for the present CrFeNi-based alloys can be summarized as follows: phase chemistry and elemental partitioning establish local electrochemical contrast; this contrast may produce spatially heterogeneous interfacial electrochemical responses; chloride exposure activates localized dissolution at the less stable regions and selected phase-adjacent areas; and the morphology and connectivity of the FCC/BCC regions determine how these local reactions are distributed and coupled across the electrode. Al/Ti addition changes the first two levels by creating a precipitation-containing multiphase architecture and, in the present tests, lowers the area-averaged corrosion kinetics relative to AC-CrFeNi. Subsequent rolling reorganizes the nominally identical alloy into a lamellar morphology, while potentially changing other microstructural variables; the HR condition is accompanied by a more capacitive interfacial response, lower i_{corr}, and much higher low-frequency impedance.

4. Conclusions

In this work, the effects of phase heterogeneity and microstructural morphology on the chloride corrosion behavior of CrFeNi-based multi-principal element alloys were systematically investigated by comparing AC-CrFeNi, AC-CrFeNiAlTi, and HR-CrFeNiAlTi. Al/Ti alloying transformed the single-phase FCC CrFeNi into an FCC/BCC heterogeneous architecture containing hierarchical ordered precipitates, which reduced the corrosion current density and increased the low-frequency impedance, indicating suppressed overall electrochemical reaction kinetics. However, post-electrochemical characterization revealed that localized corrosion remained associated with specific phase regions or phase-adjacent areas, demonstrating that phase heterogeneity improves global corrosion resistance while simultaneously introducing local electrochemical differences. At an unchanged nominal composition, hot rolling reorganized the equiaxed FCC/BCC regions into a directional lamellar morphology, leading to a further decrease in corrosion kinetics and a substantial enhancement of impedance response. The improved corrosion resistance of the lamellar structure is attributed not to a simple physical barrier effect, but to the modification of phase continuity, interfacial distribution, and spatial coupling of chemically distinct regions, which collectively alter interfacial relaxation behavior and localized corrosion evolution. These findings demonstrate that chloride corrosion in CrFeNi-based MPEAs is governed by the coupled effects of phase chemistry and microstructural organization, providing a strategy for designing heterogeneous alloy architectures with simultaneously optimized mechanical and corrosion properties.

Supplementary Materials

The additional data and information can be downloaded at: https://media.sciltp.com/articles/others/2611161119367500/HEME-26100005-SM-FC-done.pdf. Table S1. Full-frequency circuit fitting and model-sensitivity comparison. Figure S1. Experimental and fitted HR-CrFeNiAlTi impedance spectra: (a) Nyquist spectra: raw measurements compared with the 1RQ and unconstrained 2RQ fits; (b) Bode impedance magnitude; (c) Bode phase angle; (d) Relative complex residuals, including constrained 2RQ sensitivity test.

Author Contributions

Q.G.: methodology, formal analysis, writing—original draft, funding acquisition, conceptualization; C.C.: software, investigation, formal analysis; J.W.: investigation, formal analysis, funding acquisition; H.H.: investigation, formal analysis; X.Y.: writing—review & editing, validation, investigation, formal analysis. All authors have read and agreed to the published version of the manuscript.

Funding

This research was funded by the Natural Science Foundation of Hubei Province, grant numbers 2026AFB389 (Q.G.) and 2026AFC0747 (J.W.).

Institutional Review Board Statement

Not applicable.

Informed Consent Statement

Not applicable.

Data Availability Statement

The data that support the findings of this study are available from the corresponding author upon reasonable request.

Conflicts of Interest

The authors declare no conflict of interest.

Use of AI and AI-Assisted Technologies

During the preparation of this work, the authors used OpenAI ChatGPT to assist with English-language editing and to improve the schematic representation of the Graphical Abstract. After using this tool, the authors reviewed and verified the content and take full responsibility for the published article.

References

1. Ghorbani, M.; Li, Z.; Qiu, Y.; et al. Current Progress in Aqueous Corrosion of Multi-Principal Element Alloys. *Metall. Mater. Trans. A* **2024**, *55*, 2571–2588. https://doi.org/10.1007/s11661-024-07473-x.
2. Qin, Y.; Fu, J.; Lu, Z.; et al. Research Progress on Corrosion Mechanism of High-Entropy Alloys. *Trans. Nonferrous Met. Soc. China* **2026**, *36*, 1365–1387. https://doi.org/10.1016/s1003-6326(25)67036-1.
3. Ghorbani, M.; Laleh, M.; Gharbi, O.; et al. Aqueous Corrosion of Additively Manufactured Multi Principal Element Alloys: A Critical Review. *npj Mater. Degrad.* **2025**, *9*, 159. https://doi.org/10.1038/s41529-025-00701-8.
4. Zhang, J.Y.; Xiao, B.; Chou, T.H.; et al. High-Entropy Alloys: A Critical Review of Aqueous Corrosion Behavior and Mechanisms. *High Entropy Alloys Mater.* **2023**, *1*, 195–259. https://doi.org/10.1007/s44210-023-00021-z.
5. Blades, W.H.; Redemann, B.W.Y.; Smith, N.; et al. Tuning Chemical Short-Range Order for Stainless Behavior at Reduced Chromium Concentrations in Multi-Principal Element Alloys. *Acta Mater.* **2024**, *277*, 120209. https://doi.org/10.1016/j.actamat.2024.120209.
6. Sur, D.; Smith, N.C.; Connors, P.F.; et al. Investigating the Synergistic Benefits of Al on Cr(III) in the Passive Films of FeCoNi-Cr-Al CCAs in Sulfuric Acid. *Electrochim. Acta* **2025**, *513*, 145523. https://doi.org/10.1016/j.electacta.2024.145523.
7. Kang, K.W.; Li, A.X.; Zhang, B.R.; et al. Corrosion Resistance of Ultra-High Yield Strength CoCrNi-Based Medium Entropy Alloy. *J. Alloys Compd.* **2025**, *1036*, 181770. https://doi.org/10.1016/j.jallcom.2025.181770.
8. Liu, L.; Lu, K.; Jing, Z.; et al. Simultaneously Improving Strength and Corrosion Resistance of CoCrNi-Based Multi-Principal Element Alloys via Alloying with Mo Content. *J. Alloys Compd.* **2025**, *1010*, 177119. https://doi.org/10.1016/j.jallcom.2024.177119.
9. Yu, K.P.; Feng, S.H.; Ding, C.; et al. Improving Anti-Corrosion Properties of CoCrFeMnNi High Entropy Alloy by Introducing Si into Nonmetallic Inclusions. *Corros. Sci.* **2022**, *208*, 110616. https://doi.org/10.1016/j.corsci.2022.110616.
10. Yen, C.C.; Lin, S.Y.; Ting, C.L.; et al. Passivation Mechanisms of CoCrFeNiMox (X = 0, 0.1, 0.2, 0.3) High Entropy Alloys and MP35N in 3.5 wt% NaCl Aerated Aqueous Solutions. *Corros. Sci.* **2024**, *228*, 111812. https://doi.org/10.1016/j.corsci.2023.111812.
11. Zhang, M.; Shi, X.; Li, Z.; et al. Corrosion Behaviors and Mechanism of $CrFeNi_2$ Based High-Entropy Alloys. *Corros. Sci.* **2022**, *207*, 110562. https://doi.org/10.1016/j.corsci.2022.110562.
12. Zhao, Q.; Pan, Z.; Wang, X.; et al. Corrosion and Passive Behavior of $Al_xCrFeNi_{3-X}$ (X = 0.6, 0.8, 1.0) Eutectic High Entropy Alloys in Chloride Environment. *Corros. Sci.* **2022**, *208*, 110666. https://doi.org/10.1016/j.corsci.2022.110666.
13. Wang, Y.; Li, G.; Li, H.; et al. Effect of Aging on Corrosion Resistance of $(FeCoNi)_{86}Al_7Ti_7$ High Entropy Alloys. *Corros. Sci.* **2024**, *227*, 111717. https://doi.org/10.1016/j.corsci.2023.111717.
14. Cheng, H.; Luo, H.; Wang, X.; et al. Microstructure and Corrosion Resistance Properties of $(FeCoNi)_{86}Al_7Ti_7$ High-Entropy Alloy via Different Aging Time. *Corros. Sci.* **2024**, *226*, 111670. https://doi.org/10.1016/j.corsci.2023.111670.
15. Qi, W.; Wang, W.; Yang, X.; et al. Effects of Al and Ti Co-Doping on the Strength-Ductility- Corrosion Resistance of CoCrFeNi-AlTi High-Entropy Alloys. *J. Alloys Compd.* **2022**, *925*, 166751. https://doi.org/10.1016/j.jallcom.2022.166751.

16. Liu, S.; Duan, J.; Zhang, M.; et al. Correlation of Microstructure, Mechanical Properties and Corrosion Behavior in a $Ni_{34}Co_{28}Cr_{28}Al_{10}$ Multi-Principal Element Alloy with Outstanding Corrosion Resistance. *Corros. Sci.* **2024**, *228*, 111835. https://doi.org/10.1016/j.corsci.2024.111835.
17. Inman, S.B.; Han, J.; Wischhusen, M.A.; et al. Passivation and Localized Corrosion Resistance of $Al_{0.3}Cr_{0.5}Fe_2Mo_xNi_{1.5}Ti_{0.3}$ Compositionally Complex Alloys: Effect of Mo Content. *Corros. Sci.* **2024**, *227*, 111692. https://doi.org/10.1016/j.corsci.2023.111692.
18. Duan, J.M.; Jiang, Z.N.; Zeng, X.Q.; et al. Unveiling the Underlying Corrosion/Corrosion-Resistance Mechanism of a Novel Corrosion-Resistant High Entropy Alloy by Experimental Means and AIMD Simulations. *Corros. Sci.* **2024**, *227*, 111782. https://doi.org/10.1016/j.corsci.2023.111782.
19. Li, X.; Zhang, G.; Lei, N.; et al. Corrosion Behaviors of $CrFeNiNb_x$ Medium Entropy Alloys with Hypereutectic and Hypoeutectic Structures. *Mater. Today Commun.* **2023**, *35*, 106153. https://doi.org/10.1016/j.mtcomm.2023.106153.
20. Shi, X.; Li, G.; Zhang, M.; et al. Laves Phase Assisted the Passive Behaviors of Co-Free Non-Equiatomic Cr-Fe-Ni-Nb Eutectic High-Entropy Alloys. *J. Alloys Compd.* **2023**, *960*, 170905. https://doi.org/10.1016/j.jallcom.2023.170905.
21. Ao, P.; Liu, L.; Xi, Z.; et al. Coupled Effects of FCC/BCC Phase Morphology and Passive-Film Defects on the Corrosion Behavior of $Al_xFeNiCrCo$ High-Entropy Alloys. *J. Alloys Compd.* **2026**, *1080*, 190428. https://doi.org/10.1016/j.jallcom.2026.190428.
22. Wu, H.; Xie, J.; Yang, H.; et al. Corrosion Behavior and Corrosion Resistance Mechanism of a Multi-Level Heterogeneous Lamellar Structure Eutectic High Entropy Alloy. *Corros. Sci.* **2025**, *256*, 113172. https://doi.org/10.1016/j.corsci.2025.113172.
23. Xu, M.K.; Li, A.X.; Kang, K.W.; et al. Influence of Thermomechanical Processing on Microstructure, Mechanical Response and Corrosion Behavior of a Precipitation-Strengthened CoCrNi Base Alloy. *J. Alloys Compd.* **2025**, *1039*, 183290. https://doi.org/10.1016/j.jallcom.2025.183290.
24. Hong, L.; Li, H.; Huang, M.; et al. Enhancing Mechanical Property and Corrosion Resistance of $Al_{0.3}CoCrFeNi_{1.5}$ High Entropy Alloy via Grain Boundary Engineering. *Mater. Charact.* **2024**, *217*, 114420. https://doi.org/10.1016/j.matchar.2024.114420.
25. Gao, Q.; Kou, Z.; Zhou, C.; et al. Exceptional Strength-Ductility Synergy in a Casting Multi-Principal Element Alloy with a Hierarchically Heterogeneous Structure. *Mater. Today* **2024**, *81*, 70–83. https://doi.org/10.1016/j.mattod.2024.10.009.
26. Stern, M.; Geary, A.L. Electrochemical Polarization: I. A Theoretical Analysis of the Shape of Polarization Curves. *J. Electrochem. Soc.* **1957**, *104*, 56. https://doi.org/10.1149/1.2428496.
27. Brug, G.J.; van den Eeden, A.L.G.; Sluyters-Rehbach, M.; et al. The Analysis of Electrode Impedances Complicated by the Presence of a Constant Phase Element. *J. Electroanal. Chem. Interfacial Electrochem.* **1984**, *176*, 275–295. https://doi.org/10.1016/s0022-0728(84)80324-1.
28. Hirschorn, B.; Orazem, M.E.; Tribollet, B.; et al. Determination of Effective Capacitance and Film Thickness from Constant-Phase-Element Parameters. *Electrochim. Acta* **2010**, *55*, 6218–6227. https://doi.org/10.1016/j.electacta.2009.10.065.
29. Wang, X.Z.; Hu, Q.; Zhang, L.; et al. The Influence of Nb Addition on the Passivity of $CoCrNiNb_x$ Multi-Principal Element Alloys. *J. Electroanal. Chem.* **2022**, *908*, 116107. https://doi.org/10.1016/j.jelechem.2022.116107.
30. Sun, Y.; Lv, Y.; Di, J.; et al. Correlating Microstructure, Corrosion Behavior and Wear Resistance in an Additively Manufactured Heterogeneous CoCrNi-Based Medium Entropy Alloy with Outstanding Mechanical Properties. *Mater. Charact.* **2026**, *231*, 115941. https://doi.org/10.1016/j.matchar.2025.115941.
31. Wang, D.; Lei, X.; Bai, Y.; et al. Effect of La Addition on the Corrosion Behaviors of CrCoNi Medium Entropy Alloy in Chloride Solution. *Appl. Surf. Sci.* **2025**, *699*, 163164. https://doi.org/10.1016/j.apsusc.2025.163164.
32. Xie, R.; Wei, Y.; Luo, K.; et al. Effect of Environmental Factors on the Corrosion Behavior of CoCrNi and CoCrFeMnNi Alloys in 3.5 wt% NaCl Solution. *J. Mater. Res. Technol.* **2025**, *35*, 2994–3007. https://doi.org/10.1016/j.jmrt.2025.01.227.
33. Wu, Y.; Yue, Y.; Yan, X.; et al. Mechanical and Corrosion Behavior of $CoCrFeNiAl_{0.3}$ High Entropy Alloy Seamless Tubes. *J. Alloys Compd.* **2025**, *1010*, 177143. https://doi.org/10.1016/j.jallcom.2024.177143.
34. Che, C.; Jiang, M.; Li, A.; et al. Effect of Ni Content on the Corrosion Resistance of $CoCr_{0.8}FeTi_{0.4}Ni_x$ High Entropy Alloys in 3.5 wt% NaCl Solution. *J. Alloys Compd.* **2025**, *1016*, 178900. https://doi.org/10.1016/j.jallcom.2025.178900.
35. Chahlaoui, Y.; Saeidlou, S.; Al-Harbi, L.M.; et al. Bayesian-Optimized Surface Energy Microstructure-Informed Model of Active Dissolution in CrMnFeCoNi High-Entropy Alloys. *Mater. Today Commun.* **2025**, *49*, 113741. https://doi.org/10.1016/j.mtcomm.2025.113741.
36. Wang, Z.; Fu, J.; Feng, Y.; et al. Corrosion Behavior and Antifouling Performance of $CoCrFeNiCu_x$ High-Entropy Alloys in 3.5 wt% NaCl Solution. *Electrochim. Acta* **2026**, *553*, 148303. https://doi.org/10.1016/j.electacta.2026.148303.
37. Xie, C.; Han, J.; Sun, F.; et al. The Spontaneous Passivation of Multi Principal Element Alloys II: The Effect of Mn in the CoCrFeNiMn Family. *Corros. Sci.* **2025**, *244*, 112642. https://doi.org/10.1016/j.corsci.2024.112642.
38. Hou, Y.; Dou, B.; Xie, C.; et al. On the Corrosion Resistance of the CoCrFeMnNi High Entropy Alloys in Chloride-Containing Sulfuric Acid Solutions. *Appl. Surf. Sci.* **2025**, *681*, 161487. https://doi.org/10.1016/j.apsusc.2024.161487.

39. Sur, D.; Inman, S.B.; Anderson, K.L.; et al. Factors Governing Passivation Behavior of Fe-Cr-Al-Ti Alloys in Sulfate Containing Acidified Solutions: Uncovering the Many Roles of Ti. *Materialia* **2025**, *39*, 102370. https://doi.org/10.1016/j.mtla.2025.102370.
40. Wei, L.; Qin, W.M.; Chen, J.Y.; et al. $L2_1$-Strengthened Face-Centered Cubic High-Entropy Alloy with Well Pitting Resistance. *Corros. Sci.* **2023**, *215*, 111043. https://doi.org/10.1016/j.corsci.2023.111043.
41. Wang, J.; Jiang, H.; Chang, X.; et al. Effect of Cu Content on the Microstructure and Corrosion Resistance of $AlCrFeNi_3Cux$ High Entropy Alloys. *Corros. Sci.* **2023**, *221*, 111313. https://doi.org/10.1016/j.corsci.2023.111313.
42. Song, L.; Hu, W.; Liao, B.; et al. Corrosion Behavior of $AlCoCrFeNi_{2.1}$ Eutectic High-Entropy Alloy in Cl^- Containing Solution. *J. Alloys Compd.* **2023**, *938*, 168609. https://doi.org/10.1016/j.jallcom.2022.168609.
43. Tsai, F.Y.; Pandaleon, A.; O'Brien, S.; et al. Effects of Annealing on Phase Transformation and Corrosion Mechanism of Severely Deformed $Al_{0.3}CoCrFeNi$ High-Entropy Alloy. *npj Mater. Degrad.* **2026**, *10*, 109. https://doi.org/10.1038/s41529-026-00818-4.
44. Qiu, X.; Liu, X.; Pan, X.; et al. Corrosion and Tensile Performance of a $Co_{40}Cr_{20}Ni_{30}Al_{4.5}Ti_5Mo_{0.5}$ High-Entropy Alloy under High Temperature and Pressure CO_2 Environment. *J. Alloys Compd.* **2025**, *1036*, 181905. https://doi.org/10.1016/j.jallcom.2025.181905.
45. Fu, Y.; Wen, M.; Cao, Y.; et al. Enhanced Pitting Resistance of $Al_{0.4}Cr_{0.9}FeNi_{2.2}V_{0.2}$ High-Entropy Alloy via Coherent Nanoprecipitates Design. *Corros. Sci.* **2026**, *259*, 113491. https://doi.org/10.1016/j.corsci.2025.113491.